PERGAMON

International Journal of Heat and Mass Transfer 42 (1999) 1757–1773

International Journal of HEAT and MASS TRANSFER

Finite-rate chemistry in modelling of two-dimensional jet premixed CH_4/air flame

X. Zhou*, G. Brenner, T. Weber, F. Durst

Lehrstuhl für Strömungsmechanik, Universität Erlangen-Nürnberg, D-91508 Erlangen, Germany

Received 25 November 1997; in final form 17 August 1998

Abstract

This paper presents numerical simulations of two-dimensional laminar methane/air premixed jet flames with a detailed chemical kinetics mechanism. Comprehensive transport and thermodynamic physical properties for each species and gas mixture are included and the nonunity Lewis number has been taken into account for a nonuniform burning pattern of fuel-rich premixed flames. The focal point of this work is to demonstrate the sensitivity of the modelling of the detailed chemical kinetics on the flame temperature and concentrations of major components for three different equivalence ratios. The temperature and major species distributions are in good agreement with the experimental measurements by Nguyen et al., but the CO, OH and NO radical species profiles still deviate from experiments. The typical flame structure of the steady jet premixed methane/air flame has been obtained. © 1998 Elsevier Science Ltd. All rights reserved.

Nomenclature

A_{f_j} pre-exponential factor in the forward rate constant of the jth reaction
B_{f_j} temperature exponent in the forward rate constant of the jth reaction
c_p mean specific heat at constant pressure
c_{p_i} specific heat at constant pressure of the ith species
C_i molar concentration of the ith species
D_{ij} binary mass diffusivity
D_{im} effective molecular diffusion coefficient
E_{f_j} activation energy in the rate constant of the jth reaction
h mean specific enthalpy of a mixture
h_i specific enthalpy of the ith species
$h^0_{f_i}$ heat formation of the ith species at reference temperature
k_{b_j} backward rate constant of the jth reaction
k_{f_j} forward rate constant of the jth reaction
K_{C_j} equilibrium constant for the jth chemical reaction
Le_i local Lewis number of the ith species
M_i molecular weight of the ith species
N_r number of elementary chemical reactions
N_s number of gaseous species
R universal gas constant
R_{b_j} backward rate of progress of the jth reaction
R_{f_j} forward rate of progress of the jth reaction
S_L laminar flame velocity
S_ϕ source terms in the general transport equation
t time
T temperature
u, v velocity components
X_1, X_2, X_3 axial locations
x, r cylindrical axial and radial coordinates
Y_i mass fraction of the ith species.

Greek symbols

α_{ij} third body efficiency of the ith species in the jth reaction
Γ general diffusion coefficient in the general transport equation
Δt time interval
λ mixture-averaged thermal conductivity
μ mixture-averaged viscosity
v'_{ij} stoichiometric coefficient of the ith reactant species in the jth reaction
v''_{ij} stoichiometric coefficient of the ith product species in the jth reaction

* Corresponding author. Tel.: 0044 0171 975555; fax: 0044 0181 9833052; e-mail: x.zhou@qmw.ac.uk

0017–9310/98/$ - see front matter © 1998 Elsevier Science Ltd. All rights reserved
PII: S0017–9310(98)00284–1

ρ density
ϕ general variable
$\dot{\omega}_i$ net rate of reaction of the ith species by chemical reaction
$\dot{\omega}_i^+$ production rate of the ith species by chemical reaction
$\dot{\omega}_i^-$ destruction rate of the ith species by chemical reaction.

Subscripts
b backward
f forward
i species index
j reaction index
ref reference state.

1. Introduction

Premixed jet flames have been widely applied in household and industrial process heating systems since they produce flames with intense combustion. The natural gas, mainly composed of methane, is considered to be an abundant and relatively clean-burning fuel in the nature. Numerical investigations of premixed flames have been the subject of extensive research over many years because they are very important in understanding the flame structures and the chemical-physical combustion process. The reduction of NO_x emissions is expected to be an important object and stringent requirement in the near future.

Most of the jet premixed flame calculations are based on the asymptotic [1, 2] or one-dimensional analysis in which the flame structure (i.e. preheat zone, inner layer and postflame zone) may be assumed or the local Lewis number and the flame curvature may not be provided.

The global one-step chemical mechanism still plays an important role in understanding the chemical and physical process of combustion of the hydrocarbon fuels in two- and three-dimensional reacting flows. But this approach is unable to predict the thermodynamic equilibrium species (e.g. CO, H_2) for incomplete reactions, and therefore the total extent of production is overpredicted. Due to the development of computer technology, it is now possible to consider multi-elementary chemical reactions. The importance of detailed chemical kinetics has been demonstrated by theoretical and numerical analysis [3–5].

Mizimoto et al. [6] studied the Bunsen flames of hydrocarbons and hydrogen experimentally. It has been observed that, for lean methane/air mixture the maximum flame temperature across a radial section is less than the adiabatic temperature and decreases with flame height leading to the so called 'tip-opening' phenomenon, while for the rich flame the maximum temperature increases towards the tip resulting in a 'tip-closed' burning phenomenon. Katta and his coworkers have simulated and analysed the H_2/air jet premixed and diffusion flames in great detail using finite-rate chemistry [7–10]. They got the same phenomena and concluded that the local nonunity Lewis number was responsible for the temperature distributions around the tip of premixed flame. The laminar jet diffusion flames of H_2/N_2–air and $H_2/CH_4/N_2$–air have also been investigated by Takagi et al. [11, 12]. The boundary layer type conservation equations were solved and the preferential diffusion effects of heat and species were found to be important in the temperature characteristics. Both Katta and Takagi et al. suggested that the preferential effects caused the tip-open phenomenon.

The CH_4/air Bunsen premixed flame [13] still needs to be investigated numerically in order to understand the burning velocity (or height of inner cone) and the peak temperature under different conditions and by using different combustion models. Some experimental measurements [14, 15] have been obtained of such flames which supply a sound foundation for numerical simulations. It is to be noted that Nguyen et al. have reported an accurate database for the atmospheric pressure fuel-rich CH_4/air Bunsen laminar flames [15], which have not been simulated using detailed kinetics mechanism and two-dimensional full elliptic equations until now to the author's knowledge.

A detailed understanding of the interaction between the complex, finite-rate chemistry and multi-dimensional fluid dynamics are made possible by the development of numerical combustion models. The stiff source terms of the species equations require special attention in the calculations of chemically reacting flows with multiple elementary reactions. A semi-implicit integration method has been successfully applied to ensure a stable and converged solution. In the present study, numerical simulations have been implemented on axisymmetric laminar jet premixed methane/air flames at three fuel-rich equivalence ratios under atmospheric pressure, by using detailed chemistry model and multi-component diffusion. In the present simulations, the thermodynamic and chemistry data from CHEMKIN are used.

The multi-dimensional analysis in the present work includes no assumptions concerning the flame structure. Fundamental insight in the basic chemical phenomenon has been gained for the well-known Bunsen burner with methane as fuel of laminar flame.

2. Combustion model

Consider N_r elementary reactions involving N_s gaseous species A_i as follows

$$\sum_{i=1}^{N_s} \nu'_{ij} A_i \rightleftharpoons \sum_{i=1}^{N_s} \nu''_{ij} A_i, \quad j = 1, \ldots, N_r \tag{1}$$

where v''_{ij} and v'_{ij} are the ith species stoichiometric constants for the jth forward and backward reaction, respectively.

The conservation equation for chemical species i is as follows

$$\frac{\partial}{\partial t}(\rho Y_i)+\frac{\partial}{\partial x_j}(\rho u_j Y_i)=\frac{\partial}{\partial x_j}\left(\rho D_{im}\frac{\partial Y_i}{\partial x_j}\right)+\dot{\omega}_i \quad (i=1,N_s-1) \tag{2}$$

where Y_i is the mass fraction of each chemical species (here including H_2, O_2, H_2O, (N_2), O, H, OH, HO_2, CH_4, CH_3, CH_2O, HCO, CO, CO_2, N, NO for CH_4/air flames). D_{im} is the mixture diffusion coefficient of species and $\dot{\omega}_i$ is the net rate of creation of species i by chemical reaction and is given by

$$\dot{\omega}_i=\dot{\omega}_i^+-\dot{\omega}_i^- \tag{3}$$

where $\dot{\omega}_i^+$ and $\dot{\omega}_i^-$ are production and destruction rates of species i as follows:

$$\dot{\omega}_i^+ = M_i\sum_{j=1}^{N_r}(v''_{ij}R_{f_j}+v'_{ij}R_{b_j}) \tag{4}$$

$$\dot{\omega}_i^- = M_i\sum_{j=1}^{N_r}(v'_{ij}R_{f_j}+v''_{ij}R_{b_j}) \tag{5}$$

where M_i is the molecular weight of the ith species, and the forward and reverse reaction rates are

$$R_{f_j}=k_{f_j}\prod_{i=1}^{N_s}C^{v'_{ij}},\quad R_{b_j}=k_{b_j}\prod_{i=1}^{N_s}C^{v''_{ij}} \tag{6}$$

where $C_i=\rho Y_i/M_i$ is the molar concentration. The forward reaction rate constant is given by the modified Arrhenius law

$$k_{f_j}=A_{f_j}T^{B_{f_j}}e^{-E_{f_j}/RT}. \tag{7}$$

The reverse rate constant k_{b_j} is related to the forward rate constant k_{f_j} as follows

$$k_{b_j}=\frac{k_{f_j}}{K_{C_j}} \tag{8}$$

where K_{C_j} is the equilibrium constant.

When a third body exists in the chemical reaction, the forward and backward rate-of-progress variables R_{f_j} and R_{b_j} are modified as

$$R_{f_j}=\left(\sum_{i=1}^{N_s}\alpha_{ij}C_i\right)k_{f_j}\prod_{i=1}^{N_s}C^{v'_{ij}},\quad R_{b_j}=\left(\sum_{i=1}^{N_s}\alpha_{ij}C_i\right)k_{b_j}\prod_{i=1}^{N_s}C^{v''_{ij}} \tag{9}$$

where α_{ij} is the third body efficiency for the ith species in the jth reaction.

A detailed chemistry mechanism has been considered for the present methane/air premixed flames. It contains 29 elementary reactions and 13 species which is selected from refs [3, 16]. It has been investigated suitable for a broad range of equivalence ratios from fuel-lean to fuel-rich flames. The pre-exponential factor A_{f_j}, the activation energy E_{f_j} and the temperature exponent of the pre-exponential factor B_{f_j} are obtained from refs [3, 16] and listed in Table 1 for convenience. All species act equally as third bodies and the enhanced effective third body efficiency is equal to unity when a third body is required in the reaction.

Two kinds of reduced chemical mechanisms (11 reactions) have been given in ref. [16] for fuel-lean and fuel-rich premixed methane/air flames on the basis of above full mechanism containing 29 chemical reactions. The first reduced mechanism A which only consists of 2, 4, 7, 9, 13, 15, 17, 18, 20, 24, 28 is for fuel-lean flame. The reduced mechanism B consisting of 1, 4, 6, 9, 10, 15, 17, 18, 20, 21, 28 is for fuel-rich flame.

In order to consider the pollution effects, three other reactions representing nitric oxide mechanism are included [17]. The reaction scheme and the rate constants are listed in Table 2. Here only thermal NO mechanism is incorporated in the chemical-kinetics model and is predicted by the simpler Zel'dovich mechanism.

The density of species mixture can be calculated by the state equation of ideal gases. The enthalpy for chemically reacting flows is given as weighted sum of each species mass fraction

$$h=\sum_{i=1}^{N_s}Y_ih_i=\sum_{i=1}^{N_s}Y_i\left(h_{fi}^0+\int_{T_{ref}}^{T}c_{pi}\,dT\right) \tag{10}$$

where $h_{f_i}^0$ is the heat formation of the ith species at the reference temperature T_{ref} (=298.16 K). The integral part is the sensible heat.

The energy equation of enthalpy is written as

$$\frac{\partial}{\partial t}(\rho h)+\frac{\partial}{\partial x_j}(\rho u_j h)=\frac{\partial}{\partial x_j}\left(\frac{\lambda}{c_p}\frac{\partial h}{\partial x_j}\right)+\frac{\partial}{\partial x_j}\left[\frac{\lambda}{c_p}\sum_{i=1}^{N}h_i(Le_i^{-1}-1)\frac{\partial Y_i}{\partial x_j}\right] \tag{11}$$

where Le_i is the local Lewis number of i species defined as

$$Le_i=\frac{\lambda}{c_p}\frac{1}{\rho D_{im}}. \tag{12}$$

The last term in the enthalpy equation is caused by preferential diffusion of species. The Soret effect of the thermal-diffusion effect are neglected in the analysis.

The temperature of the gas mixture can be implicitly calculated by solving equation (10) using a Newton–Raphson method because the specific heat c_{p_i} of the species is strongly dependent on temperature. The solution is refined until an accuracy is achieved within a prescribed criteria.

In addition to the above species and energy equations of concern, the basic N–S conservation equations of mass and momentum are well-known and not listed here. The details can be found in ref. [8]. The gravity effect must be

Table 1
Chemical kinetics for $CH_4/O_2/N_2$ combustion
$k_{f_j} = A_{f_j} T^{B_{f_j}} \exp(-E_{f_j}/RT)$, $R = 1.987$ cal (mol^1 K^{-1})

j	Reactions considered	A_{f_j} (mol, cm, s)	B_{f_j}	E_{f_j} (cal mol^{-1})
1	$CH_4+H \rightleftharpoons CH_3+H_2$	2.24E+04	3.0	8740.0
2	$CH_4+OH \rightleftharpoons CH_3+H_2O$	2.20E+13	0.0	4965.0
3	$CH_4+O \rightleftharpoons CH_3+OH$	1.26E+14	0.0	11 900.0
4	$CH_3+O \rightleftharpoons CH_2O+H$	2.00E+14	0.0	2000.0
5	$CH_3+O_2 \rightleftharpoons CH_2O+OH$	1.00E+11	0.0	10 000.0
6	$CH_2O+H \rightleftharpoons HCO+H_2$	1.25E+10	1.0	3200.0
7	$CH_2O+OH \rightleftharpoons HCO+H_2O$	4.80E+13	0.0	0.0
8	$CH_2O+O \rightleftharpoons HCO+OH$	5.00E+13	0.0	4570.0
9	$CH_2O+M \rightleftharpoons CO+H_2+M$	2.00E+16	0.0	37 000.0
10	$HCO+H \rightleftharpoons CO+H_2$	2.00E+14	0.0	0.0
11	$HCO+OH \rightleftharpoons CO+H_2O$	1.00E+14	0.0	0.0
12	$HCO+O \rightleftharpoons CO+OH$	3.00E+11	1.0	500.0
13	$HCO+O_2 \rightleftharpoons CO+HO_2$	3.00E+13	0.0	0.0
14	$HCO+M \rightleftharpoons CO+H+M$	5.00E+12	0.0	–19 000.0
15	$CO+OH \rightleftharpoons CO_2+H$	2.50E+12	0.0	5700.0
16	$CO+O+M \rightleftharpoons CO_2+M$	3.60E+15	−1.0	2500.0
17	$H_2+OH \rightleftharpoons H_2O+H$	2.20E+13	0.0	5144.0
18	$H+O_2 \rightleftharpoons O+OH$	2.20E+14	0.0	16 780.0
19	$H_2+O \rightleftharpoons OH+H$	1.80E+10	1.0	8900.0
20	$H+O_2+M \rightleftharpoons HO_2+M$	1.40E+13	0.0	−1000.0
21	$H+HO_2 \rightleftharpoons 2OH$	2.00E+14	0.0	2000.0
22	$H+HO_2 \rightleftharpoons H_2O+O$	5.00E+13	0.0	1000.0
23	$H+HO_2 \rightleftharpoons H_2+O_2$	6.00E+13	0.0	2000.0
24	$OH+HO_2 \rightleftharpoons H_2O+O_2$	4.00E+13	0.0	0.0
25	$O+HO_2 \rightleftharpoons OH+O_2$	6.00E+13	0.0	0.0
26	$OH+H+M \rightleftharpoons H_2+M$	2.30E+19	−2.0	0.0
27	$H+O+M \rightleftharpoons OH+M$	6.20E+13	−0.6	0.0
28	$2OH \rightleftharpoons H_2O+O$	6.30E+12	0.0	1090.0
29	$2H+M \rightleftharpoons H_2+M$	2.00E+16	−1.0	0.0

Table 2
NO pollution mechanism

j	Reactions considered	A_{f_j} (mol, cm, s)	B_{f_j}	E_{f_j} (cal mol^{-1})
30	$N_2+O \rightleftharpoons NO+N$	1.82E+14	0.0	76 241.0
31	$N+O_2 \rightleftharpoons NO+O$	6.46E+09	1.0	6280.0
32	$O_2+N_2 \rightleftharpoons 2O+N_2$	3.56E+18	−1.0	118 000.0

included in the source term of a momentum equation when the experimental set is vertically installed. The general form of the transport equation for the two-dimensional transient axisymmetric laminar reactive flow can be written as

$$\frac{\partial}{\partial t}(\rho\phi)+\frac{\partial}{\partial x}(\rho u\phi)+\frac{1}{r}\frac{\partial}{\partial r}(r\rho v\phi) = \frac{\partial}{\partial x}\left(\Gamma\frac{\partial\phi}{\partial x}\right)+\frac{1}{r}\frac{\partial}{\partial r}\left(r\Gamma\frac{\partial\phi}{\partial r}\right)+S_\phi \quad (13)$$

where ϕ denotes 1, u, v, h, Y_i and the general diffusion coefficient Γ is in turn 0, μ, μ, λ/c_p and D_{im}, respectively. Temperature- and species-dependence are imposed in the thermodynamic and transport property calculations. The mixture viscosity μ and the mixture thermal conductivity λ are based on Wilke and Wassiljewa equation [18]. The thermal conductivity and the viscosity of individual species are estimated from the Chapman–Enskog collision theory. The mixture-averaged specific heat c_p is the sum of specific heat of each species c_{p_i} weighted by mass frac-

tion and c_{p_i} is a temperature-dependent polynomial approximation. The effective molecular diffusion coefficient D_{im} is a function of mole fraction and binary mass diffusivity D_{ij} of each species, and D_{ij} is obtained using the Chapman–Enskog equation and the Lennard–Jones characteristic parameters.

3. Numerical schemes

Time-dependent, axisymmetric Navier–Stokes equations are solved along with the species and energy-conservation equations. The Cartesian velocity components are stored in a collocated grid system. The general forms of equation (13) represent conservation equations for overall mass, axial and radial momentums, enthalpy, mass fraction of species in cylindrical coordinates. The equations are solved separately with the SIMPLE method to couple the pressure and velocity. At first, the axial and radial momentum equations are solved. After pressure corrections being calculated the velocities and pressure are corrected in order to satisfy the continuity equation. The enthalpy transport equation is then solved and the temperature can be decoded from enthalpy and species by Newton–Raphson method. Then the chemical species equations are handled sequentially in the order of H_2, O_2, H_2O, (N_2), O, H, OH, HO_2, CH_4, CH_3, CH_2O, HCO, CO, CO_2, N, NO for the methane/air flame. It satisfies the condition that no quenching occurs. If radicals diffuse faster than they are generated through the chemical release, then the flame slowly quenches because the heat-release rate depends on the local concentration of radical species such as H, O and OH, etc. The species N_2 can be directly obtained by the global species conservation law. Finally, the thermochemical and transport properties are decoded from the CHEMKIN-II package and serve as new properties for the next iteration. This process is repeated until a prescribed convergence criterion is achieved.

The finite volume integration of the transport equation (13) is linearized and then the resulting algebraic equation is solved by the Strongly Implicit Procedure (SIP) method [19]. A relaxation technique can be used to ensure a converging solution especially at the initial time steps. The relaxation factor for the species equation is much lower than for the other dependent equations. Calculation of flames using finite rate chemistry is quite difficult mainly due to the fact that the heat-release rate (or reaction progress) depends on the local concentrations of radical species such as H, O, OH and the reactants.

The source term of the reaction rates in a species equation is treated in a special way. The production terms of the reaction rates are treated explicitly while the destruction terms are treated implicitly in order to maintain the diagonal dominance of the resulting systems of equations and to guarantee the convergence of the solution procedure. This semi-implicit method is necessary for a stable integration of the solution for multi-elementary reactions with multi-component species.

Four kinds of boundary conditions are considered in the calculations. Besides the primary and secondary inlets, axisymmetric line and outlet, a pressure boundary condition is imposed at the unconfined air entrainment boundary.

The numerical modeling procedure for combusting flows is as follows: the isothermal flow solutions are first obtained and used as initial conditions for the combusting flow. Then the flame is ignited by setting the species mass fractions and temperature equal to that at adiabatic equilibrium state at the inner tube rim of 0.5 mm thickness above the primary exit. The adiabatic equilibrium temperature is 1996 K and the adiabatic equilibrium mole fractions for flame A are listed in Table 3. At some grid points near the primary inlet, the temperature is temporarily increased to about 1000 K during the first 10 time steps. The flame can be initiated and propagate towards downstream with the enhancement of diffusion of equilibrium species and heat. At the beginning of the calculation a small time step (e.g. $\Delta t = 0.1$ s) is accepted to allow a suitable temperature resolution for flame ignition. The adiabatic equilibrium condition at the tube rim is removed after the flame reaches a relatively steady state. Finally, the time step can be increased to 10 s to accelerate the convergence.

4. Results and discussion

The flames analysed are stabilized on a vertically mounted methane/air Bunsen burner which is similar to the one described by Nguyen et al. [15]. A 17 mm-diameter (D_1) central fuel tube is surrounded by a 70 mm-diameter (D_2) air coflow matrix. Three kinds of fuel-rich CH_4/air Bunsen flames have been conducted at the equivalence ratio of 1.38, 1.52 and 1.70, referred to as flame A, B and C. Table 4 shows the working conditions for the present three flames, where slm is the unit of volume flux rate of litre per minute, e.g. 1 slm $= (10^{-3}/60)$ $\mathrm{m^3\,s^{-1}}$. The volume flow rate of the air coflow V_3 is equal to 82 slm in all cases, which means an equal coflow velocity. The volume flow rate at the primary inlet, i.e. the sum of the volume rate of the CH_4 stream V_1 and that of air stream V_2, is slightly different; 7.66 slm for flame A, 7.68 slm for flame B and 7.74 slm for flame C. The average velocity u_1 at the primary inlet and the surrounding coflow velocity u_2 can be obtained from

$$u_1 = \frac{4(V_1+V_2)}{\pi D_1^2}, \quad u_2 = \frac{4V_3}{\pi(D_2^2-D_1^2)}. \tag{14}$$

Calculations are made on a physical domain of 300×85 mm with a 122×62 non-uniform grid system.

Table 3
Adiabatic equilibrium mole fractions

Species	H_2	O_2	H_2O	N_2	O	H
Mole fraction	5.90E−02	6.91E−07	1.77E−01	6.45E−01	5.32E−07	3.81E−04
Species	OH	HO_2	CH_4	CH_3	CH_2	HCO
Mole fraction	1.17E−04	3.29E−10	3.94E−12	2.26E−13	2.75E−09	9.53E−09
Species	CO	CO_2	N	NO		
Mole fraction	7.11E−02	4.72E−02	6.74E−10	13.2E−05		

Table 4
Premixed CH_4/air Bunsen flame working conditions

Flame	Equivalence ratio	CH_4 (slm)	Air (slm)	Coflow (slm)	u_1 (m s^{-1})	u_2 (m s^{-1})
A	1.38	0.97	6.69	82	0.56	0.38
B	1.52	1.05	6.63	82	0.56	0.38
C	1.70	1.17	6.57	82	0.57	0.38

Uniform 32 cells are concentrated within 8.5 mm radial coordinate and non-uniform cells with exponential distribution are distributed along the axial direction so that the grid points are clustered near the reaction zone (40×8.5 mm). A parabolic velocity profile is given at the primary exit of the central tube simulating a fully developed inlet flow. A uniform profile is set at the surrounding inlet stream. The grid independence is assessed by comparing different grids.

The predicted streamlines for flames A and C are shown in Figs 1 and 2. The inner cold conical zone suggests a flame height of about 40 mm for flame A while the flame height for flame C is predicted a little higher than flame A but much lower than the experimental inner flame height of 78 mm. The reason of the disagreement is discussed subsequently. Inside this cone, the radial velocity is small compared to the axial velocity and the density changes a little from that at the primary inlet stream. Rapid reactions are taking place immediately upstream the conical flame front within a luminous conical region. The burned gas molecules along the inner cone expand and change their directions from the initially parallel direction to the slating direction. The entrainment of annulus air which dilutes and cools the burned gases converges the streamlines to the outer cone.

The laminar flame velocity can be approximately deduced from equation (2) of ref. [7] under the assumption of straight conical surface

$$\overline{S_L} = \frac{2\sin\theta}{h}\int_0^h u\left(1-\frac{x}{h}\right)\mathrm{d}x \tag{15}$$

where u is the local axial flow velocity of unburned gases at each integration axial position x, θ is the half value of the inner cone angle, h is the inner flame height. The flame speed is proportional to the inverse of inner conical length. The laminar flame speed is an important physical–chemical parameter of a combustible mixture in premixed flames, because it contains the basic information on

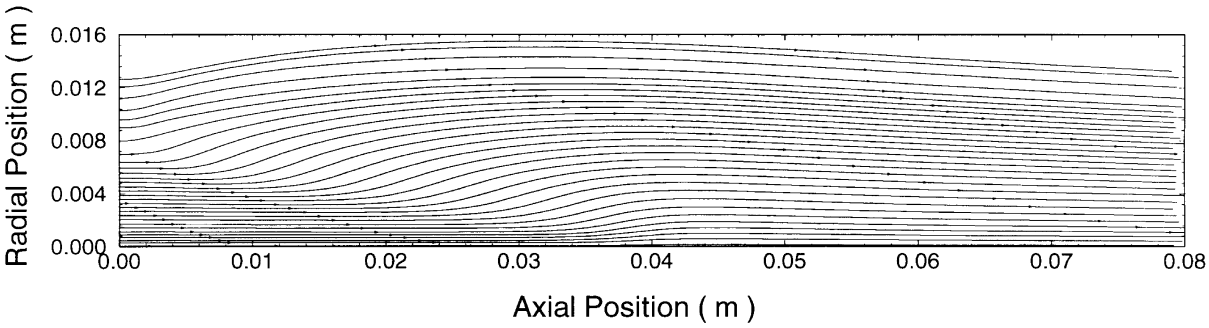

Fig. 1. Streamlines of fuel-rich premixed methane/air flame A ($\phi = 1.38$).

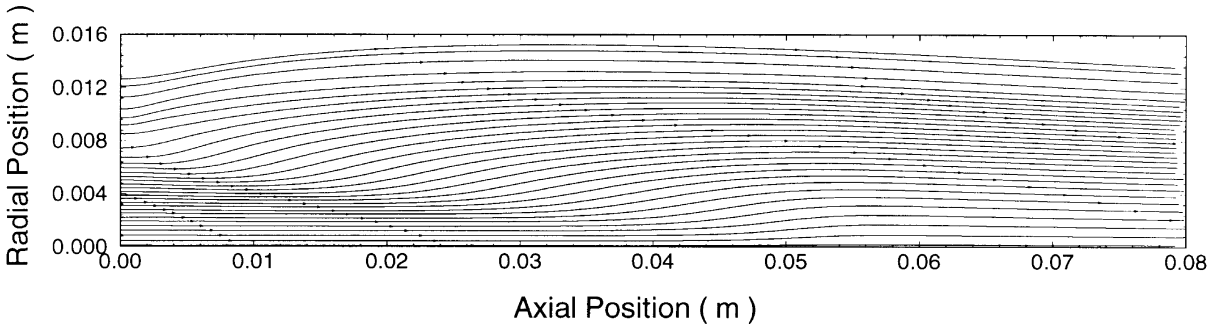

Fig. 2. Streamlines of fuel-rich premixed methane/air flame C ($\phi = 1.70$).

diffusivity and energy release rate. It is also a function of temperature increase in the preheat zone. The predicted flame velocity is about 17 cm s for flame A which compares well with the experimental data by Kee et al. [20].

The temperature contours of the jet premixed methane/air flame A are shown in Fig. 3. The predicted maximum flame temperature for this case is about 2242 K, which is a little higher than the experimental peak temperature at about 2077 K. The temperature distribution around the inner cone shows that a high-temperature region is located along the sides of the flame. The clustered contours near the conically shaped flame surface means that the fuel burns intensely in this region. It is found that in the flame a little lift-off phenomenon occurs, but the flame is to be anchored at the tube rim when the velocity profile of the secondary air inlet is parabolic rather than uniform. The distribution of NO for flame A is shown in Fig. 4. The species NO peak is about 100 ppm and located near the outer flame cone. The highest NO-concentrations are found at the downstream end of the zone of highest temperature. Mixing with the shielding air further downstream reduces the NO level due to dilution effects.

The three flames are discussed and compared with experiments in detail as follows. The experimental data for distributions of temperature, major species, CO, OH and NO are obtained from ref. [15] for laminar premixed methane/air Bunsen flames.

Figures 5 and 6 show the radial profiles of temperature and species mole fractions at X_1 axial locations ($X_1 = 21$ mm above the burner exit) by prediction and experiment. The lines correspond to the present simulations and the dots represent the experimental results of Nguyen et al. [14]. The same holds for the following graphics. It is shown that the temperature rapidly rises from the unburned conical core to approximately 2000 K and then increases a little slowly between the inner premixed flame cone and the outer flame cone. Figure 5 shows that the peak temperature is located at the surface of the outer flame zone instead of the inner flame cone surface. This is because of the preferential effect of species resulting from non-unity Lewis number. The products of H_2O and CO_2 achieve the highest values, coinciding with that, the oxygen and methane are consumed nearly totally within the double-cone region. The reaction and heat release are taking place mainly within the region between the two cones. Then the temperature decreases rapidly and recovers to the level of surrounding air outside the outer cone. The luminous zone, in which the species mole fractions of H_2, H_2O and CO_2 are higher and that of CH_4 is

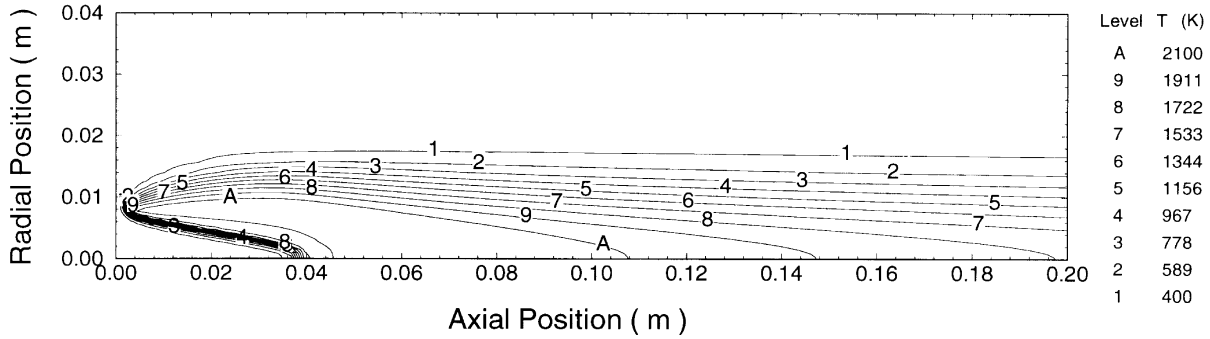

Fig. 3. Temperature distributions in the premixed methane/air flame A ($\phi = 1.38$).

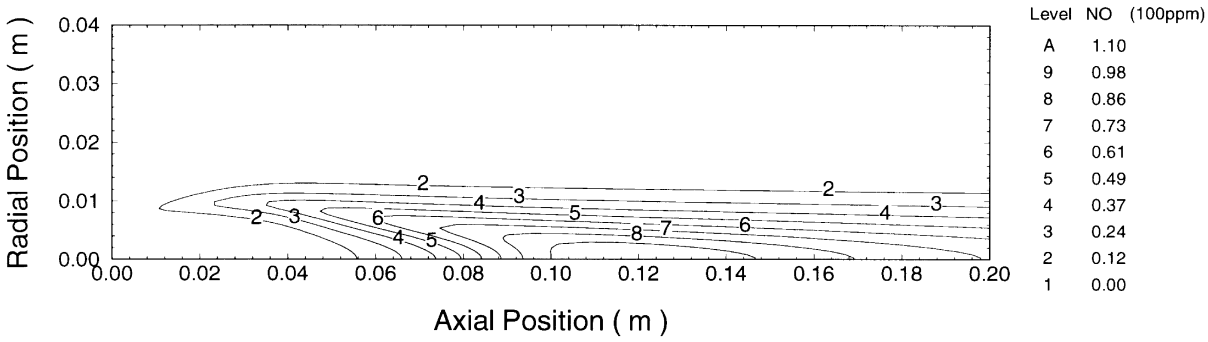

Fig. 4. NO distributions in the premixed methane/air flame A ($\phi = 1.38$).

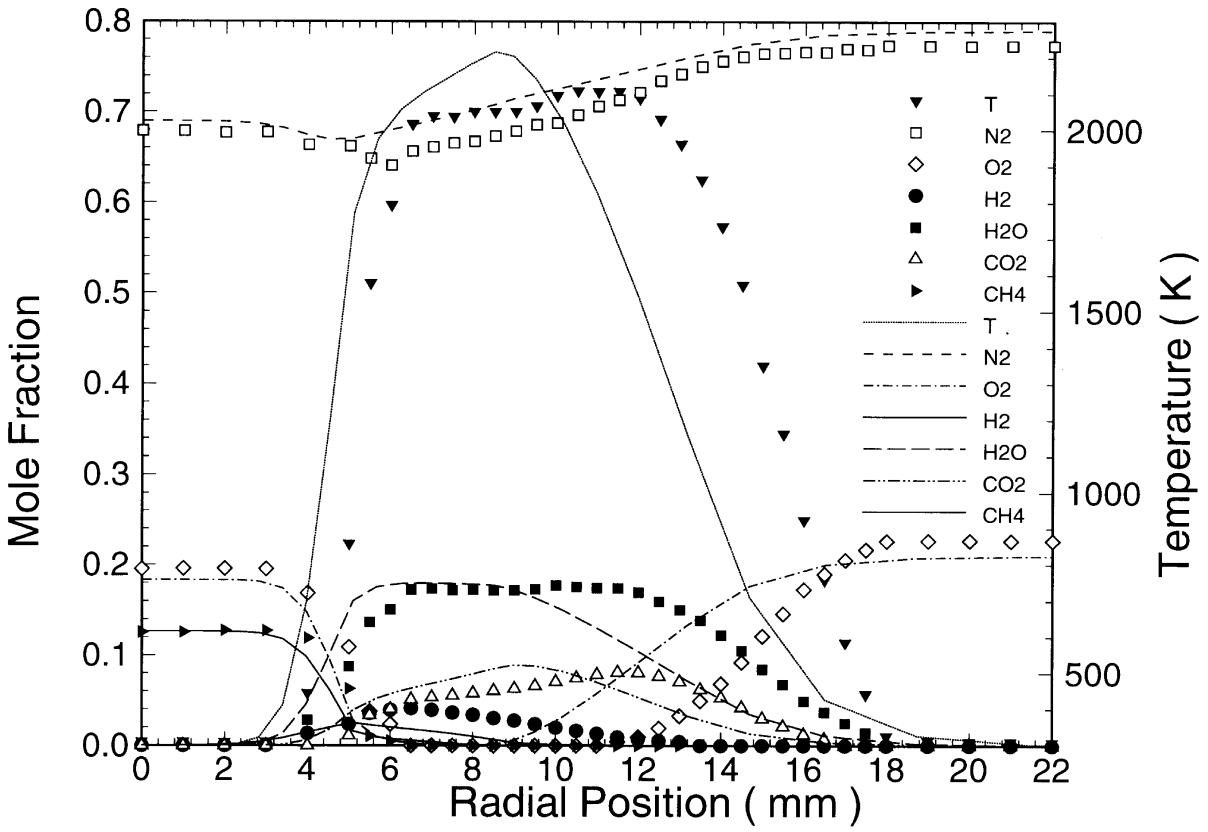

Fig. 5. Comparison of predicted and measured radial temperature and major species profiles for flame A at the X_1 (=21 mm) axial location.

zero and O_2 is consumed at most, is about 5 mm in height at this cross-section which is lower than observed in the experiment.

The predicted peak values of species CO (magnified by 10) and OH (magnified by 100) are much lower and the peak positions are a little upstream than the measured values. The disagreements might be due to the chemical mechanism. Overall, the present results exhibit the same trends as do the experiments. However, a large discrepancy of NO concentration (magnified by 10^4) is found between the prediction and measurements. There are two possible reasons. One concerns the suitability of the thermal NO mechanism, which is only applicable to high temperature above 2000 K. The prompt-NO route, which dominates at low temperature especially for fuel-rich conditions and is almost produced beyond the inner

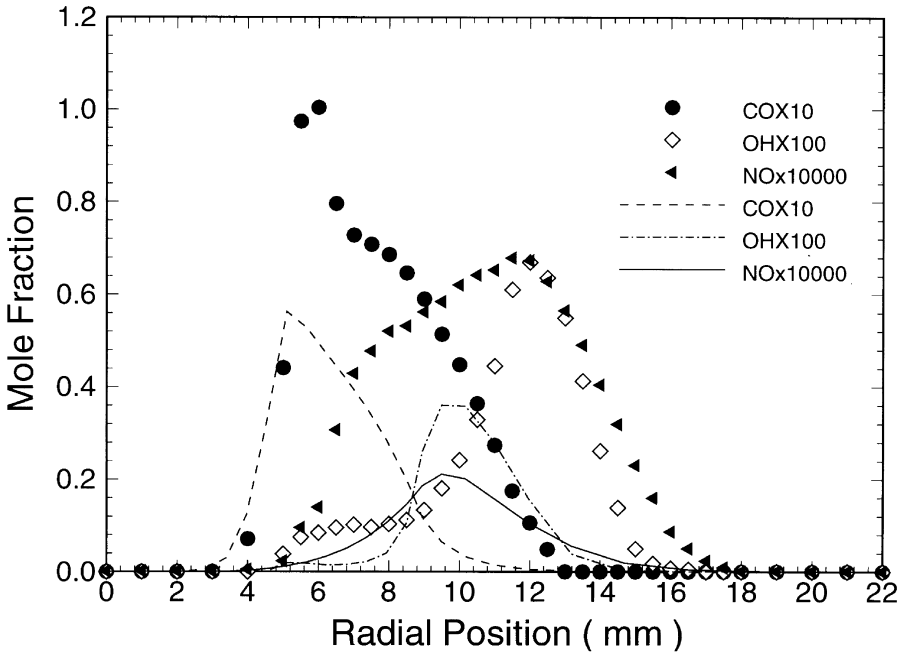

Fig. 6. Comparison of predicted and measured radial minor species profiles for flame A at the X_1 (=21 mm) axial location.

flame front, has not been considered at present. The second reason may be due to that the spatial resolution is not good enough.

Figures 7 and 8 show the comparison of predicted and measured radial temperature and species profiles for flame A at the X_2 axial location ($X_2 = 50$ mm). This location is approximately 8 mm above the tip of the inner flame cone. Figure 7 shows that all of the CH_4 has been consumed at this location. The peak temperature is the same as that of about 2200 K at X_1 location. The temperature is nearly constant between the centerline and the outer cone and then decreases rapidly from the outer flame cone towards the air entrainment boundary. The calculated position of the peak temperature along the radial direction is smaller than observed in the experiment. This results in an earlier decrease of mole fractions of species H_2O and CO_2 and earlier increase of the O_2 concentration. However, the agreements are quantitatively good. It can be seen from Fig. 8 that the mole fraction of CO concentration reaches its maximum at the centerline and decreases with radius. The predicted CO mole fraction is lower compared to the experiment especially near the centerline. The calculation also predicts a smaller radius of the peak OH concentration where the outer diffusion flame is established.

Comparisons of predicted and measured radial temperature and species profiles for flame A at the X_3 axial location ($X_3 = 90$ mm) are plotted in Figs 9 and 10. At the radical cross section, the predicted peak temperature (2242 K) is a little higher than the measured peak temperature of about 2077 K and a little lower than that by prediction at X_1 and X_2 axial locations. The agreements of the temperature and major species distributions between calculation and experiments are quite satisfactory. The peak values of species H_2O and H_2 are a little lower while the value of CO_2 concentration is higher than that at X_2 axial location. Note that the predicted peak value of NO is twice higher than the measurements shown in Fig. 10. The species OH and CO concentrations are overpredicted outside the outer flame cone in comparison with experiments.

It is noted that the predicted NO concentration compares well with experiment at the X_3 location which is about 50 mm above the tip of the inner flame cone and further away than X_1 and X_2 locations. Thus, it might be expected that prompt-NO mechanism has a great influence near the premixed flame front and the thermal mechanism mainly dominates near the diffusion flame front.

Figures 11 and 12 show the comparison of predicted and measured temperature and species distributions along the centerline of flame A. It can also be seen that the flame front position is about 40 mm in the axial direction and the flame front zone is very narrow. The bulk of the combustion products are burned rapidly in the narrow chemical reaction zone because of the exponential relationship between the chemical reaction rate and temperature. The predicted temperature peaks about 2200 K at the visible outer cone flame tip. The oxygen concentration increases slowly beyond the outer cone along with the decrease of temperature. The methane con-

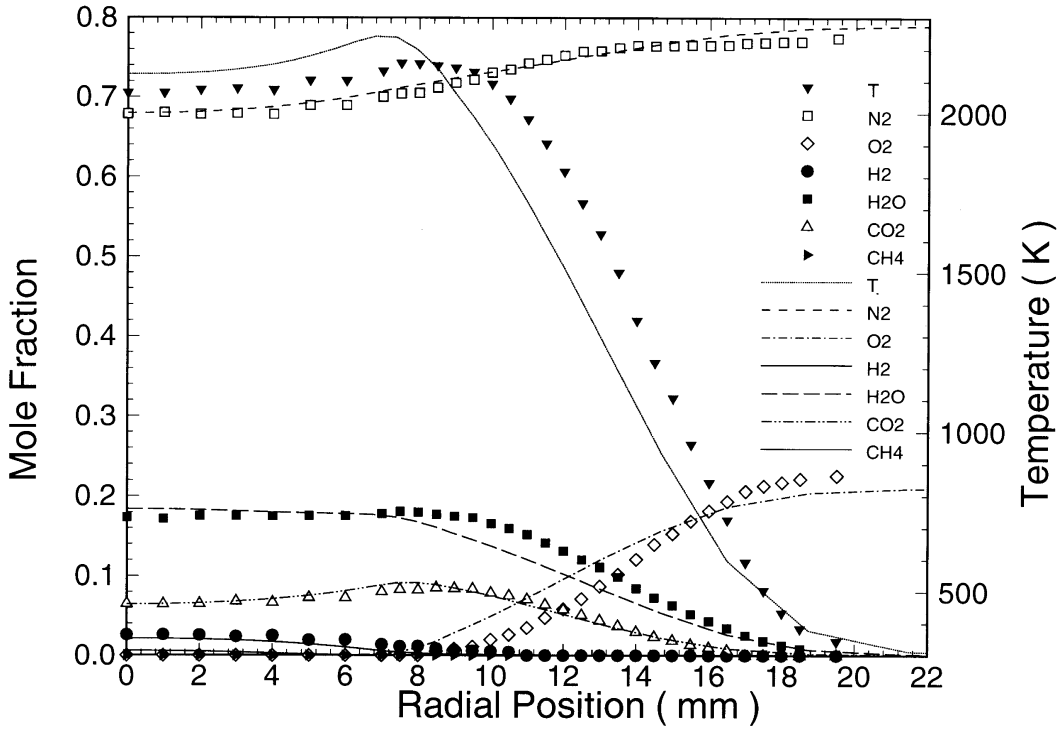

Fig. 7. Comparison of predicted and measured radial temperature and major species profiles for flame A at the X_2 (=50 mm) axial location.

centration stays to be zero behind the flame front towards the outlet. It is to be said that there exists an outer diffusion flame zone where the oxygen flowing out of the secondary inlet can diffuse into the burned gases and react with chemical products.

The agreement between the experiment and present calculations is satisfactory for the temperature and major species distributions. But there still exists a larger discrepancy for the minor species such as OH, CO and NO. The predicted peak temperature is about 2100 K at the diffusion flame front but the temperature peaks at the premixed flame front by experiment. The position of the inner flame height is well predicted at about 42 mm above the burner exit.

The computed results predict well the general trend of the experimental profiles. The fuel species CH_4 disappears rightly after the luminous zone and the steady products H_2O and H_2 form and reach maximum values. The concentration of CO_2 reaches its maximum and that of H_2 is zero at the secondary cone flame tip where the temperature reaches another peak value and then decreases due to dilution. This is because the combustion product H_2 mixes and reacts with the surrounding air which diffuses from the annular flow into the diffusion flame zone.

The discrepancy of the concentration of NO between computation and measurement is large especially near the premixed flame front which can be seen in Fig. 12. The possible reason is the absence of prompt-NO chemistry which is important near the flame zone. The prediction also over-predicts the NO value above the outer flame cone, which may be due to the absence of thermal radiation in the simulation or due to the incorrect prediction of the radical pool by fuel breakdown mechanism. There are two peaks of mole fraction of species OH. One is at the inner flame front and the other is at the diffusion flame front. The predicted peak level is lower than measurement. The agreement of the second peak value of OH species mole fraction is good, but the OH species is under-predicted before the secondary diffusion flame front and over-predicted after the flame front.

Figures 13 and 14 show the comparison of predicted and measured temperature and major species distributions along the centerline of flame B ($\phi = 1.52$). The trends of the predicted temperature and species distributions for flame B is similar to that for flame A. The peak temperature is a little lower than flame A. The predicted inner flame cone height deviates from the experiment. The predicted flame velocity is, therefore, higher than the experimental value due to the shorter inner flame

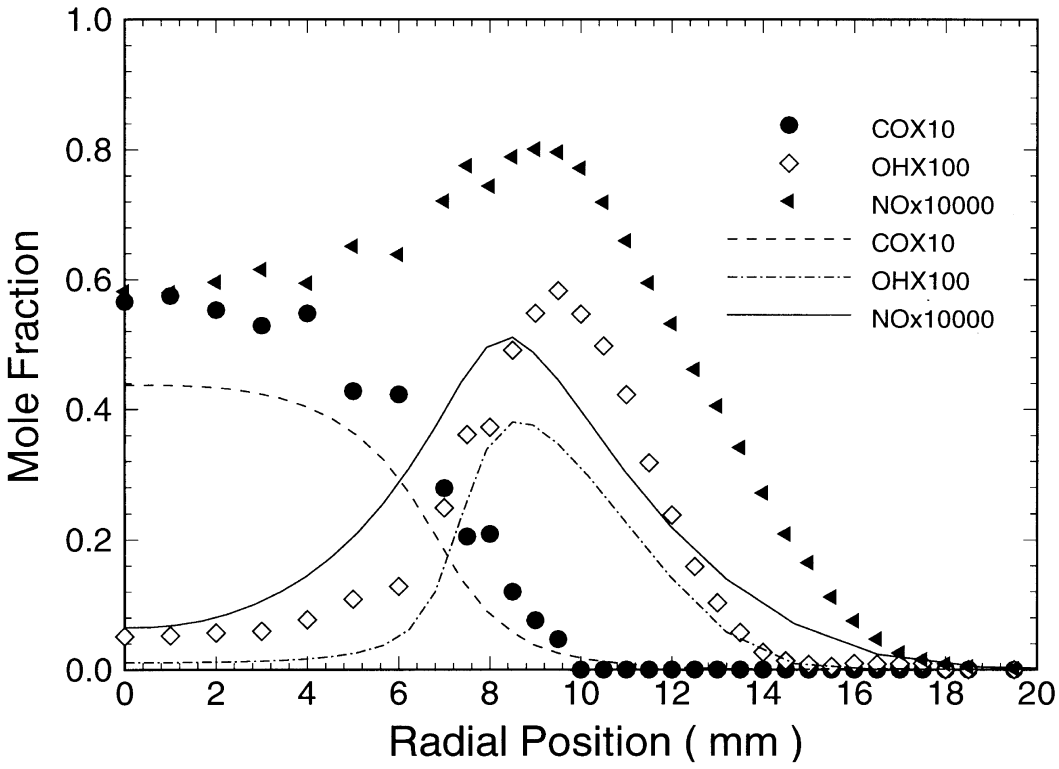

Fig. 8. Comparison of predicted and measured radial minor species profiles for flame A at the X_2 (= 50 mm) axial location.

height by prediction. Figures 15 and 16 show the similar trends for flame C, but the premixed flame height deviates a lot compared to flame B.

Above all of the three Figures of 12, 14 and 16 displaying the minor species distributions along the centerline, most phenomena are well simulated. With the increase of equivalence ratio, the peak NO mole fraction decreases and peak CO increases. CO reaches the maximum value at the tip of inner flame cone although it is under-predicted for all these flames. OH concentration peaks at the tip of outer flame cone. In general, it can be seen from Figs 11, 13 and 15 that the flame thickness (in which the temperature keeps high and flame burns intensely) increases with equivalence ratio.

Figure 17 shows the major species and temperature distributions along the centerline of flame C by different chemical mechanisms in comparison with experiments. The dots represent experimental data by Nguyen et al. The dotted lines are the predicted results by full chemical mechanisms for methane/air and the solid lines are the simulation results using the reduced mechanism B. The reduced mechanism A has also been applied to calculate the flame C, but it is found that the inner conical height is too short (meaning a much higher burning velocity) and the results are not shown in the paper. The major difference between the reduced mechanism A and B is that, in mechanism A the radical OH is mainly involved in the destruction of CH_4, CH_2O, HO_2, but H is mainly involved in the mechanism B. It can be seen that the peak temperature predicted by the reduced mechanism B is lower than by the full mechanism and the experimental data. The mechanism B also predicts an even shorter inner flame height. The concentrations of species N_2 and H_2 are over-predicted and the species H_2O is under-predicted by mechanism B. From the general point of view the full chemical mechanism predicts better than the reduced mechanism.

5. Conclusion

In this paper we report the application of multi-step elementary chemical reactions in modeling the two-dimensional premixed methane/air Bunsen flames with comprehensive physical property models and multi-component diffusion. Very stable and converged simulation solutions have been obtained by incorporating the implicit linearization of the source terms of species equations. Distributions of temperature, CO, OH, NO and the major species (N_2, O_2, H_2, H_2O, CO_2, CH_4) along

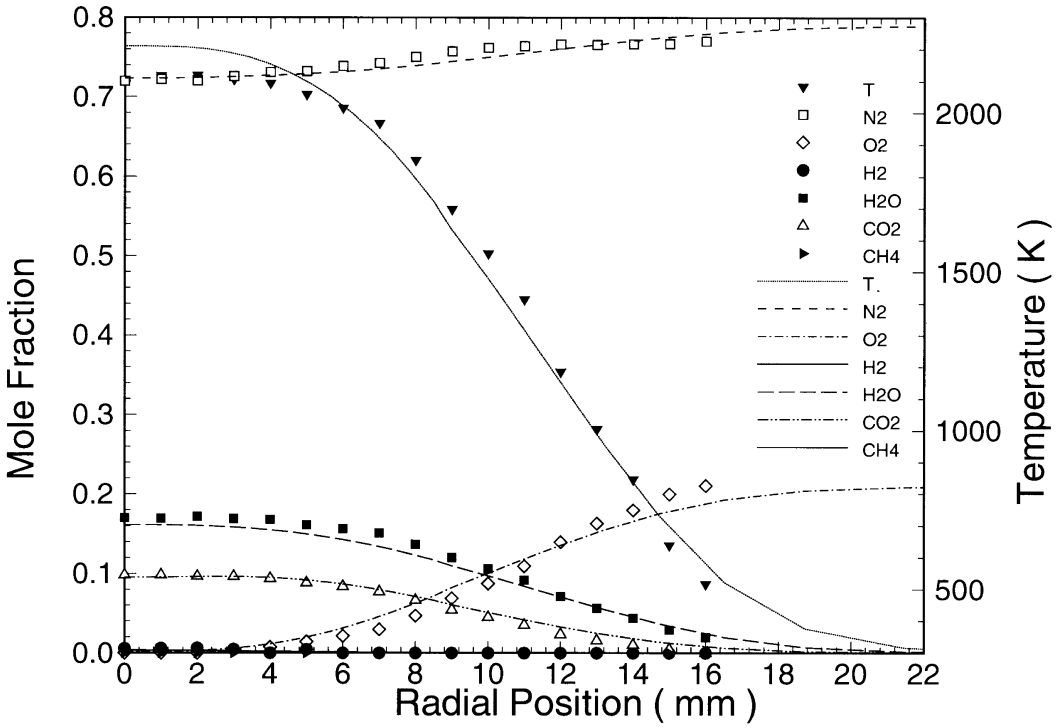

Fig. 9. Comparison of predicted and measured radial temperature and major species profiles for flame A at the X_3 (=90 mm) axial location.

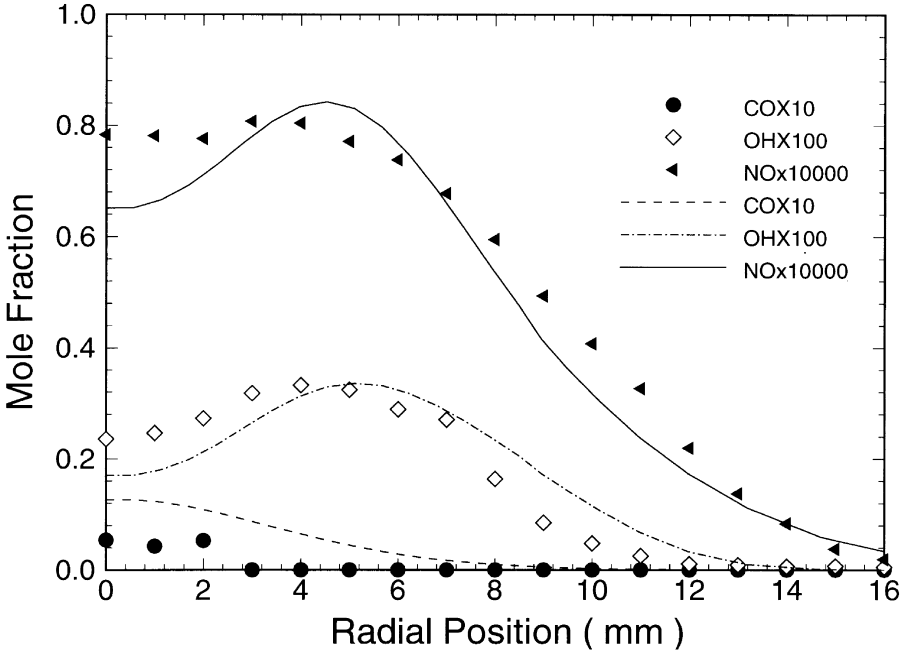

Fig. 10. Comparison of predicted and measured radial minor species profiles for flame A at the X_3 (=90 mm) axial location.

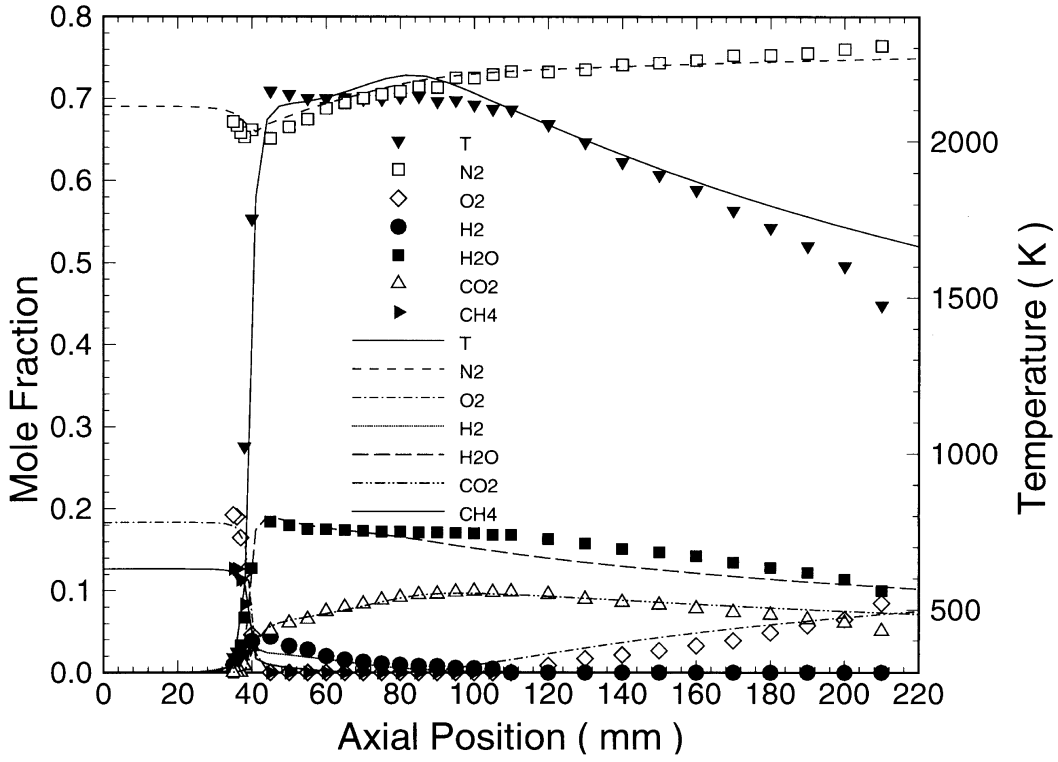

Fig. 11. Comparison of predicted and measured temperature and major species distributions along the centerline of flame A.

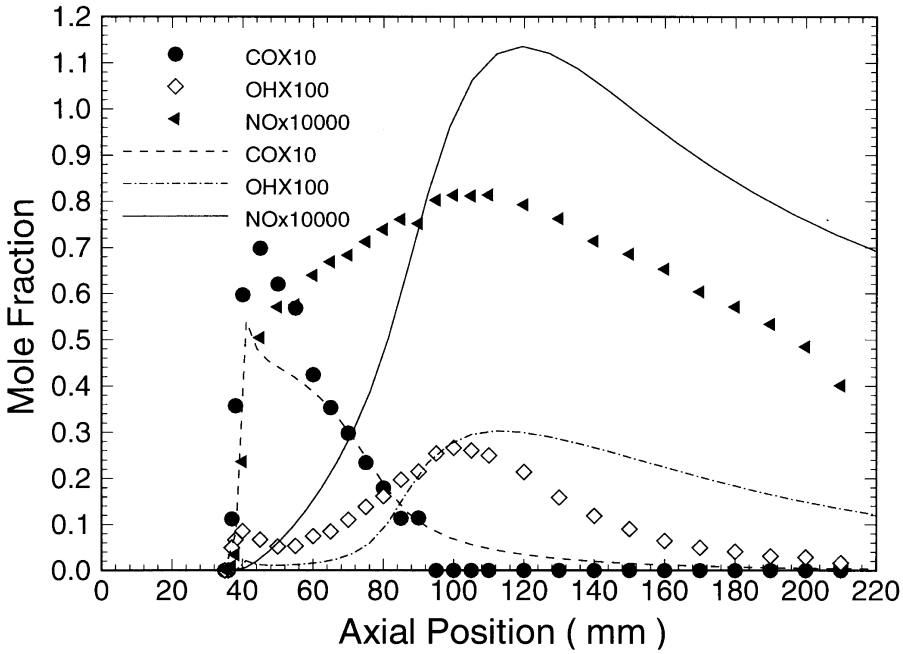

Fig. 12. Comparison of predicted and measured minor species distributions along the centerline of flame A.

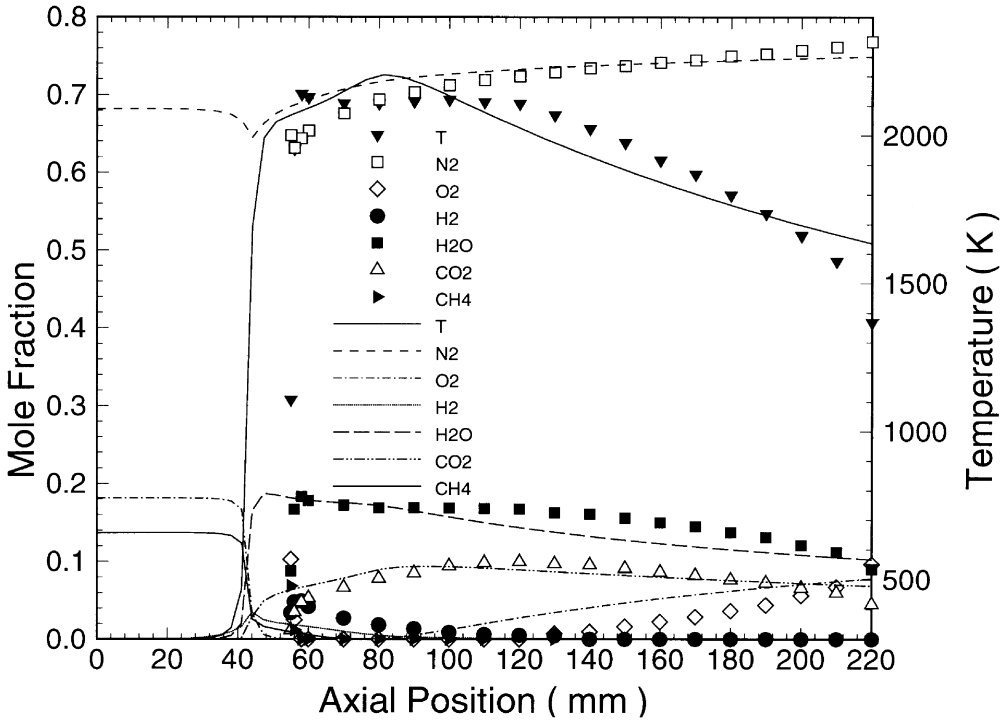

Fig. 13. Comparison of predicted and measured temperature and major species distributions along the centerline of flame B.

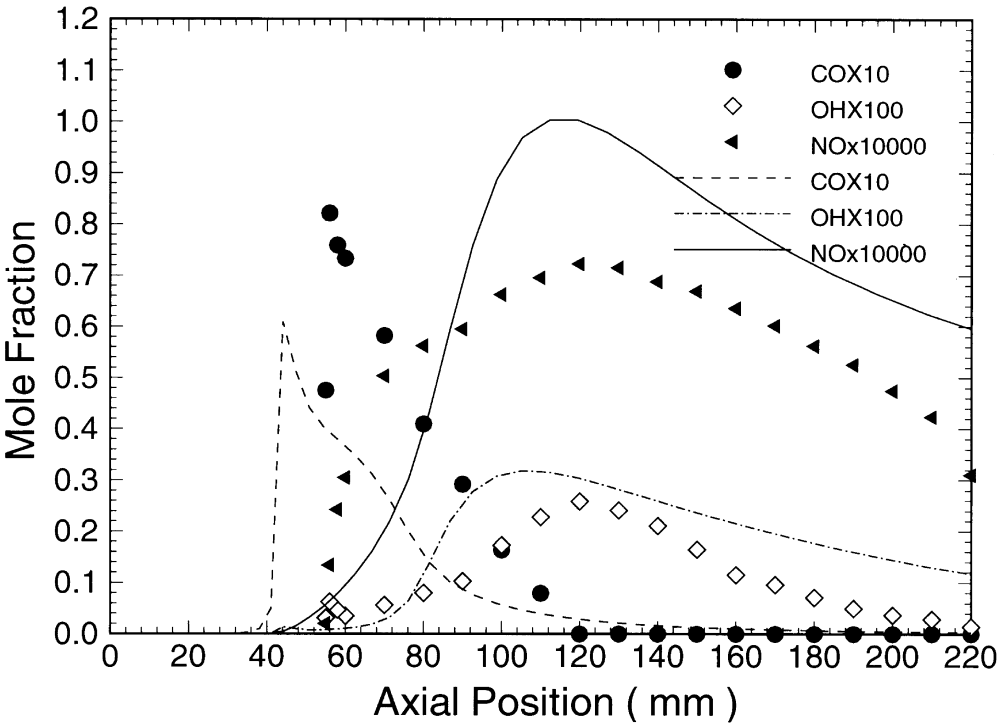

Fig. 14. Comparison of predicted and measured minor species distributions along the centerline of flame B.

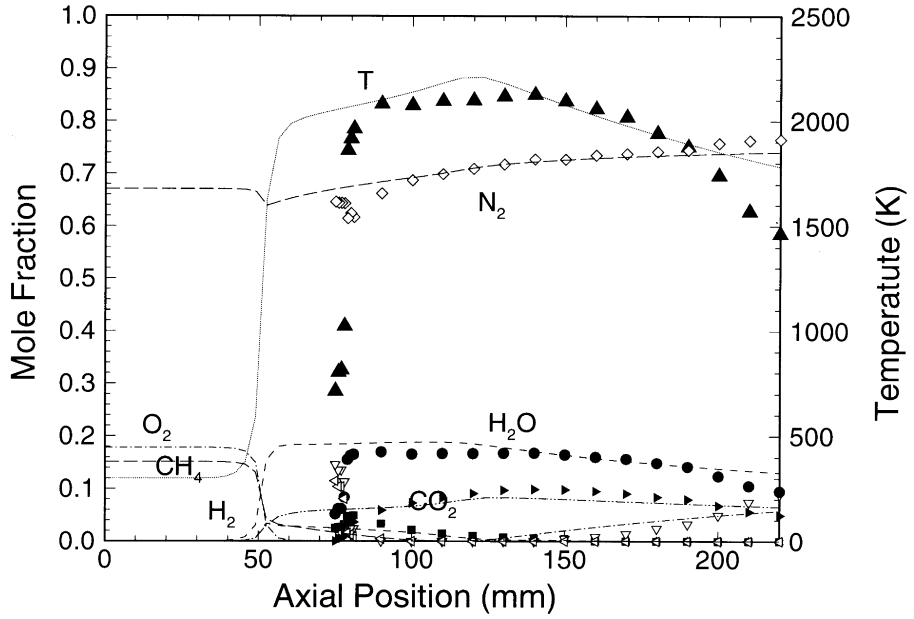

Fig. 15. Comparison of predicted and measured temperature and major species distributions along the centerline of flame C.

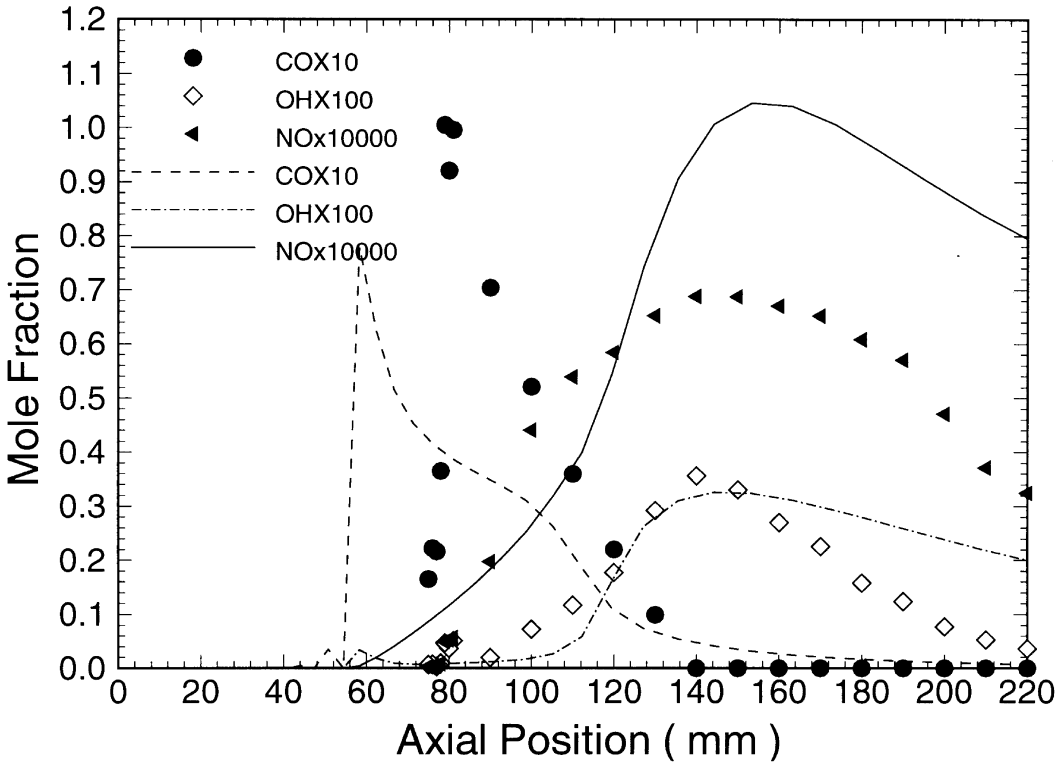

Fig. 16. Comparison of predicted and measured minor species distributions along the centerline of flame C.

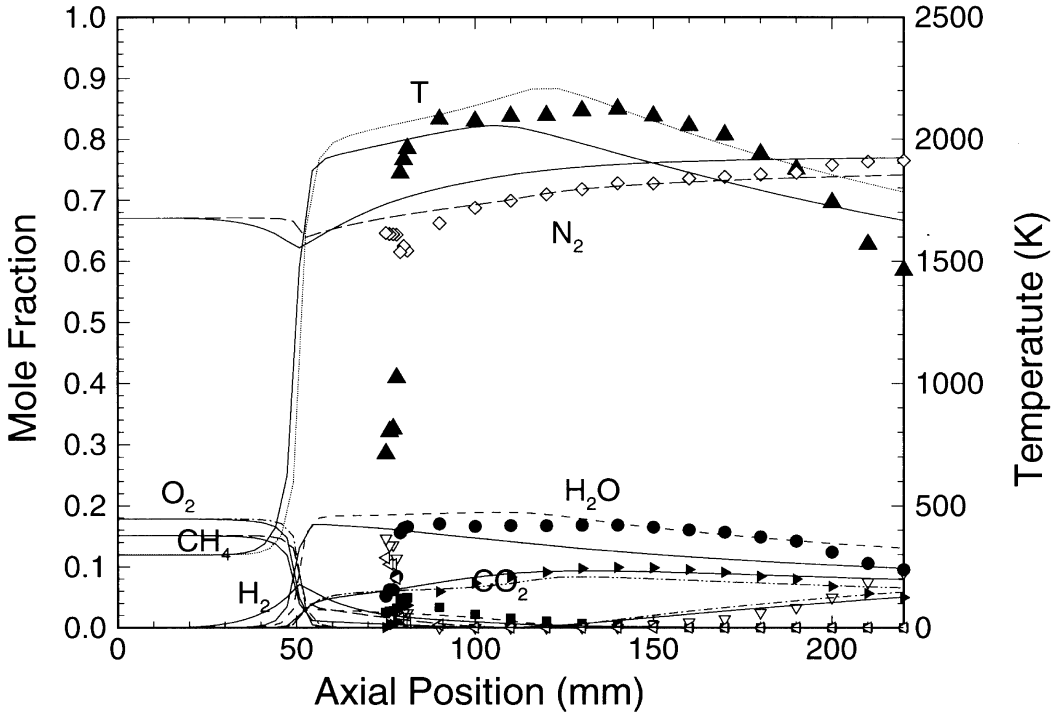

Fig. 17. Comparison of predicted and measured temperature and major species distributions along the centerline of flame C.

radial and axial directions have been numerically investigated and compared with experiments for three fuel-rich flames at equivalence ratios of 1.38, 1.52 and 1.70. The predicted results of distributions of temperature and major species concentrations are in good agreement with the measured data by Nguyen et al. [15]. The general trends for the fuel-rich flames are correctly simulated.

The predicted peak temperatures for the three flames are similar with each other at about 2200 K which is about 100 K higher than the measured peak flame temperature. The inner flame height is well predicted for flame A with the lowest equivalence ratio among the three fuel-rich flames, while the disagreement of the inner height increases with the equivalence ratio for which the inner core height is under-predicted in comparison with measured value. Thus, the present CH_4/air chemical mechanism is suitable for the prediction of fuel-rich premixed flames at a relatively low equivalence ratio. The discrepancies of NO mole fractions are large between the calculation and measurements. This is due to the absence of consideration of radiation effect and prompt-NO chemistry mechanism in the methane/air premixed jet flames. It needs to be improved further by including radiation model and more detailed NO formation mechanism in the future.

Acknowledgements

This work is supported by the Alexander von Humboldt Foundation in Germany. The authors thank Prof. Toshimi Takagi in Osaka University for very useful suggestions. The authors also thank Dr Quang-Viet Nguyen in Berkeley University for supporting the experimental database and appreciate discussions.

References

[1] M. Bui-Pham, K. Seshadri, F.A. Williams, The asymptotic structure of premixed methane–air flames with slow CO oxidation, Combustion and Flame 32 (1992) 343–362.
[2] K. Seshadri, N. Peters, F.A. Williams, Asymptotic analysis of stoichiometric and lean hydrogen–air flames, Combustion and Flame 96 (1994) 407–427.
[3] G. Tsatsaronis, Prediction of propagating laminar flames in methane, oxygen, nitrogen mixtures, Combustion and Flame 33 (1978) 217–239.
[4] C.K. Westbrook, F.L. Dryer, Chemical kinetic modeling of hydrocarbon combustion, Progress in Energy and Combustion Science 10 (1984) 1–57.
[5] T.S. Norton, K.C. Smyth, J.H. Miller, M.D. Smooke, Comparison of experimental and computed species con-

centration and temperature profiles in laminar, two-dimensional methane/air diffusion flames, Combustion Science and Technology 90 (1993) 1–34.

[6] M. Mizomoto, Y. Asaka, S. Ikai, Effects of preferential diffusion on the burning intensity of curved flames, Twentieth Symposium (International) on Combustion, The Combustion Institute, Pittsburg, 1984, pp. 1933–1939.

[7] V.R. Katta, W.M. Roquemore, Numerical studies on the structure of two-dimensional H_2/air premixed jet flame, Combustion and Flame 102 (1995) 21–40.

[8] V.R. Katta, L.P. Gross, W.M. Roquemore, Effect of non-unity Lewis number and finite-rate chemistry on the dynamics of a hydrogen–air jet diffusion flame, Combustion and Flame 96 (1994) 60–74.

[9] V.R. Katta, W.M. Roquemore, Numerical investigations of transitional H_2/N_2 diffusion flames, Combustion and Flame 32 (1994) 84–94.

[10] V.R. Katta, W.M. Roquemore, Role of inner and outer structures in transitional jet diffusion flame, Combustion and Flame 92 (1993) 274–282.

[11] T. Tagaki, Z. Xu, M. Komiyama, Preferential diffusion effects on the temperature in usual and inverse diffusion flames, Combustion and Flame 106 (1996) 252–260.

[12] T. Takagi, Z. Xu, Numerical analysis of laminar diffusion flames—effects of preferential diffusion of heat and diffusion, Combustion and Flame 96 (1994) 50–59.

[13] K.-Y.K. Kuo, Premixed laminar flames, in: Principles of Combustion, Wiley, New York, 1986, pp. 285–345.

[14] D.E. Heard, J.B. Jeffries, G.P. Smith, D.R. Crosley, LIF measurements in methane/air flames of radicals important in prompt-NO formation, Combustion and Flame 88 (1992) 137–148.

[15] Q.V. Nguyen, R.W. Dibble, C.D. Carter, G.J. Fiechtner, R.S. Barlow, Raman-LIF measurements of temperature, major species, OH and NO in methane–air bunsen flame, Combustion and Flame 105 (1996) 499–510.

[16] G. Tsataronis, Vereinfachung des Methane/Sauerstoff-Reactionsmechanismus, Brennstoff. Waerme, Kraft 30 (1978) 249–254.

[17] F.V. Bracco, Nitric oxide formation in droplet diffusion flames, Fourteenth Symposium (International) on Combustion, The Combustion Institute, Pittsburg, 1973, pp. 831–842.

[18] R.C. Reid, J.M. Prausnita, B.E. Poling, The Properties of Gases and Liquids, 4th ed., McGraw-Hill, New York, 1987.

[19] H. Stone, Iterative solution of implicit approximations of multi-dimensional partial differential equations, SIAM Journal on Numerical Analysis 5 (1968) 530–558.

[20] R.J. Kee, J.F. Grcar, M.D. Smooke, J.A. Miller, FORTRAN for modeling steady laminar one-dimensional premixed flames, Sandia Report SAND 85-8240.